

Simple Electroabsorption Calculator for Designing 1310 nm and 1550 nm Modulators Using Germanium Quantum Wells

Rebecca K. Schaevitz, Elizabeth H. Edwards, *Member, IEEE*, Jonathan E. Roth, Edward T. Fei, Yiwen Rong, Pierre Wahl, Theodore I. Kamins, *Fellow, IEEE*, James S. Harris, *Life Fellow, IEEE*, and David A. B. Miller, *Fellow, IEEE*

Abstract—With germanium showing significant promise in the design of electroabsorption modulators for full complementary metal oxide semiconductor integration, we present a simple electroabsorption calculator for Ge/SiGe quantum wells. To simulate the quantum-confined Stark effect electroabsorption profile, this simple quantum well electroabsorption calculator (SQWEAC) uses the tunneling resonance method, 2-D Sommerfeld enhancement, the variational method and an indirect absorption model. SQWEAC simulations are compared with experimental data to validate the model before presenting optoelectronic modulator designs for the important communication bands of 1310 nm and 1550 nm. These designs predict operation with very low energy per bit (<30 fJ/bit).

Index Terms—Germanium, modulators, optical interconnects, optoelectronic, quantum wells, quantum-confined Stark effect, silicon.

I. INTRODUCTION

WITH power consumption in interconnects becoming increasingly significant both on-chip and environmentally, it is important to look at possible technologies for meeting future energy targets [1]. If optical interconnects are to replace copper wires within the next decade, one study suggests optical output devices should consume <30 fJ/bit

Manuscript received August 1, 2011; revised August 29, 2011; accepted September 17, 2011. Date of current version January 24, 2012. This work was supported in part by under Agreement HR0011-08-09-0001 between DARPA and Oracle. The views expressed are those of the author and do not reflect the official policy or position of the Department of Defense or the U.S. Government. The authors acknowledge the financial support of the Interconnect Focus Center, one of the six research centers funded under the Focus Center Research Program, a Semiconductor Research Corporation program. They also acknowledge the financial support of the Intel Fellowship Program, the Stanford Graduate Fellowship, and the National Science Foundation Graduate Research Fellowship.

R. K. Schaevitz, E. H. Edwards, E. Fei, T. I. Kamins, J. S. Harris, and D. A. B. Miller are with the Department of Electrical Engineering, Stanford University, Stanford, CA 94305 USA (e-mail: rschaevitz@stanford.edu; ehe@stanford.edu; edfei@stanford.edu; kamins@stanford.edu; harris@snow.stanford.edu; dabm@stanford.edu).

J. E. Roth is with Aurrion, Goleta, CA 93117-3153 USA (e-mail: jon-roth@stanfordalumni.org).

Y. Rong is with Phillips Lumileds, San Jose, CA 95131-1008 USA (e-mail: rywryw@gmail.com).

P. Wahl is with the Department of Applied Physics and Photonics, Vrije Universiteit Brussel, Brussels 1050, Belgium (e-mail: pierrewahl@gmail.com).

Color versions of one or more of the figures in this paper are available online at <http://ieeexplore.ieee.org>.

Digital Object Identifier 10.1109/JQE.2011.2170961

and <7 fJ/bit for off-chip and on-chip communication, respectively [1]. It is particularly important to meet these demands using silicon-compatible materials so the technologies can be compatible with silicon manufacturing. The III–V compounds typically used for optoelectronics face many challenges for integration with silicon (whether using epitaxial growth, wafer-to-wafer bonding or die bonding); one example is for epitaxial growth where the groups III and V materials act as dopants in group IV materials like silicon.

Silicon-compatible optoelectronic modulators can use two possible effects: electro-refraction or electroabsorption. Commercial research has typically focussed on electro-refraction using a Mach-Zehnder interferometer (MZI) architecture [2], [3]. However, since it is difficult to make large index changes with most electro-refractive mechanisms in Si, these devices require relatively longer path lengths to achieve the required phase change (with the shortest path length $\sim 5\times$ longer than the electroabsorption modulators modeled here). Since the electro-refractive mechanisms in silicon are relatively energy-inefficient, energy consumption in such devices is relatively large, with the lowest reported energy consumption of 5 pJ/bit at 10 Gb/s [3]. Using the same mechanism, ring resonators (RR) use strong resonance to create very compact device structures. These compact devices have demonstrated energies as low as ~ 3 fJ/bit at 12.5 Gb/s [4]. However, due to this strong resonance, these devices are highly temperature sensitive and need precise temperature tuning that can easily cost an excess 100 fJ/bit [1], with the state-of-the-art fully integrated temperature controller consuming <1 mW for ± 10 °C [5].

Unlike silicon, germanium has a direct gap at 0.8 eV that is close to its indirect gap (at 0.66 eV). Consequently, Ge has demonstrated strong electroabsorption characteristics using either the Franz-Keldysh effect (FKE) [6], [7] or quantum-confined Stark effect (QCSE) [8], [9]. These effects are strong optoelectronic mechanisms and can allow for much more compact, low-power devices. Due to the ease of fabrication for the bulk-Ge based FKE devices, they have shown significant improvement in a short time and show promise for achieving the low energy per bit needed for off-chip communication. In 2008, the first demonstration of a modulator device gave 50 fJ/bit, though no high-speed results were reported [6]. More recently, these devices have demonstrated 100 fJ/bit at 12.5 Gb/s operation and 30 GHz bandwidth in a waveguide

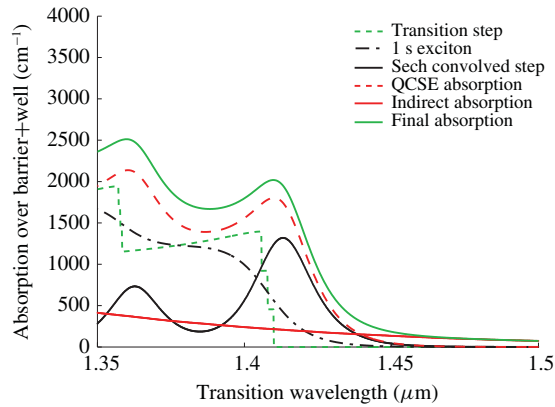


Fig. 1. Components of QCSE and indirect absorption forming SQWEAC.

integrated structure [7]. Given the band gap of Ge, these devices are limited in operation to the C-band at >1500 nm as the addition of Si (with a direct gap of 4.0 eV) to shift the band gap to shorter wavelengths quickly causes indirect absorption to dominate (thus increasing the insertion loss).

While they have only demonstrated up to 3.5 GHz operation [10], [11], Ge QCSE devices use the strongest electroabsorption mechanism available in semiconductors. With quantum-confinement in a Ge/SiGe quantum well (QW) heterostructure, the electroabsorption spectra are enhanced by both the concentration of the absorption into steps and the particularly strong excitonic enhancement that, unlike in the FKE, is retained in the presence of electric fields. This large change in absorption allows for ultra-compact, low-energy modulators in Si-compatible materials. Devices with <20 fJ/bit have been demonstrated and improvement is still expected [11].

With the expectation of meeting future energy and density requirements through QCSE in Ge QW electroabsorption modulators, it is important to have the ability to design devices in an easy and effective manner. Researchers have modeled this material system using electronic band structures defined by tunneling resonance [12], tight-binding [13], [14] and k - p [15]–[17] methods as well as approaches including excitonic effects using the variational method [16], [17] and a Green's function method [18]. Both tight-binding and k - p methods are computationally and time intensive, which is not desirable when attempting to design future devices. Tunneling resonance, however, is a fast and effective method of mapping the shift in exciton peaks with electric field if nonparabolicity is added to the Ge direct conduction band [12].

In this paper, we will build on the work from [12] to fully model the electroabsorption spectra of Ge/SiGe QWs. To do so, excitonic effects are included with 2D Sommerfeld enhancement for the above-band gap excitonic enhancement and the variational method for the below-band gap excitonic peaks [19]. Since both Si and Ge are indirect band gap materials, a model for indirect absorption is included to better simulate the expected insertion loss (IL) in this material system [20], [21]. After validating the simple quantum well electroabsorption calculator, or SQWEAC, with a range of material structures and growth conditions, we present two

possible waveguide modulator designs for operation in the important communication bands of 1310 nm and 1550 nm. Unlike for FKE, which is dominated by indirect absorption at 1310 nm, the excitonic enhancements present in Ge/SiGe QWs allow for designs at this wavelength while still maintaining strong enough extinction ratios (ER) for communication off-chip or on-chip. These designs also operate within the energy requirements for off-chip optical communication with speeds that could be >100 GHz as they are only limited by the resistance-capacitance (RC) time constant (similar to III–V devices that demonstrate speeds up to 500 Gb/s [22]).

We will begin the paper with a discussion of the models incorporated in SQWEAC. We will then describe the growth, fabrication and setup used to obtain experimental data, which is compared with SQWEAC results. Following validation of the model, we will present the two modulator designs at 1310 nm and 1550 nm.

II. THEORY

In order to model the electroabsorption spectra in Ge/SiGe QWs, we must include both QCSE with excitonic contributions as well as indirect absorption. For an in-depth discussion of the indirect absorption present in this material system, see Ref. [21]. The theoretical models that make up the QCSE spectra that contribute to the red dashed line in Fig. 1 include: (a) Transfer matrix (tunneling resonance) method for the electronic band structure as well as (b) Sommerfeld enhancement and (c) variational method for the below-band gap excitonic peak contributions.

The transfer matrix method, or tunneling resonance method (originally presented in [12]), determines the quantum confinement energies of the $\text{Ge/Si}_{1-x}\text{Ge}_x$ heterostructure using boundary conditions where Ψ and $(1/m)d\Psi/dz$ are continuous at the boundary (Ψ being the envelope wavefunction and m being the effective mass). While the number of wells varied from 10 to 60, a single QW (Fig. 2) was used to model all the QWs since the thickness and height of the barriers are sufficient to prevent quantum-mechanical coupling between QWs. The calculation method for the band gaps, offsets and masses is fully described in [12] and will not be discussed here. The results from [12] are slightly different only in the well width as the inclusion of the exciton binding energy (described later) necessitates a slight ~ 0.5 nm reduction of the fitted well width.

The simulation of the transfer matrix model at various static electric fields results in wavefunctions of the electrons (Ψ_e) and holes (Ψ_h) (which describe the probability of finding an electron and hole along the growth direction within the well) and confinement energies for all the relevant transitions and electric fields. These wavefunctions are used for the variational method, described later, as well as to determine the step height of each transition (such as electron 1 to heavy hole 1, E1-HH1). The step heights are calculated as the modulus squared of the overlap of the wavefunctions of the relevant bands involved in the transition ($|\langle\Psi_e|\Psi_h\rangle|^2$), such as wavefunctions E1 and HH1 for the E1-HH1 transition.

These step heights, which demonstrate the strength of the optical absorption, are further augmented in total magnitude due to the Coulomb attraction of the electrons and holes (the excitonic effect). The increase in absorption for photon energies above the start of the steps due to excitonic effects is described by the 2D Sommerfeld enhancement factor given in Eq. (1). Due to selection rules from the conduction to the light hole (LH) and HH bands, the E-LH transitions are reduced by a factor of three compared with the E-HH transitions with the assumption that the electric vector of light is polarized in the plane of the QWs (TE mode) [23]. These Sommerfeld enhanced steps are shown by the dashed green line in Fig. 1

$$S_{2D}(\epsilon) = \frac{2}{[1 + \exp(-2\pi/\sqrt{\epsilon})]} \quad (1)$$

$$R_y = \frac{\mu q^4}{8h^2(\epsilon_r \epsilon_0)^2} \quad (2)$$

where ϵ refers to the energy normalized in exciton Rydbergs above the start of each step, $\sqrt{(\hbar\omega - E_{step})/R_y}$. The exciton Rydberg energy for Ge is calculated with Eq. (2), where μ is the reduced effective mass between the relevant bands (such as E-HH), q is the charge of an electron, h is Planck's constant, ϵ_r is the relative permittivity and ϵ_0 is the free space permittivity [24].

Following calculation of the Sommerfeld enhanced transition step, the variational method is used to determine the strength and location in energy of the 1S exciton [23], [25], [26]. (We neglect exciton bound states other than the 1S, presuming we can effectively fold their contributions into the 1S exciton absorption in practice. No other such bound states are resolved spectrally.) Following [26], when the static electric field is applied perpendicular to the plane of the QWs (parallel to the growth direction), the energy associated with the Coulomb attraction between the electrons and holes, or the binding energy, can be represented by two summed energies, $E_B = E_{KEr} + E_{PEr}$, for the kinetic and potential energy components. The kinetic and potential energies in Joules can be represented by Eqs. (3) and (4), where $\hbar = h/2\pi$, λ is the effective Bohr-radius of the exciton, Ψ is the full wavefunction and $V_{e,h}(r, z_e, z_h)$ is the potential given in Eq. (5)

$$E_{KEr} = \frac{\hbar^2}{2\mu\lambda^2} \quad (3)$$

$$E_{PEr} = \langle \Psi | V_{e-h} | \Psi \rangle \quad (4)$$

$$V_{e,h}(r, z_e, z_h) = \frac{-q^2}{4\pi\epsilon_r\epsilon_0(|z_e - z_h|^2 + r^2)^{1/2}} \quad (5)$$

where r is the relative position of the electron and hole in the plane of the QW while z_e and z_h are the coordinates perpendicular to the plane (parallel to the growth direction).

Here we have assumed we can write the full wavefunction as separable wavefunctions that is the product of the electron (Ψ_e) and hole (Ψ_h) wavefunctions in the direction perpendicular to the layers (evaluated here by the tunneling resonance method) and a relative motion electron-hole wavefunction in the plane of the layers (U). We are assuming for variational purposes that the electron-hole wavefunction has the form of a 1S-like

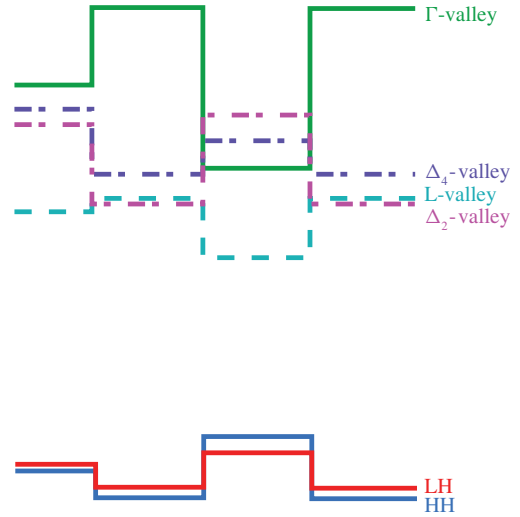


Fig. 2. Energy band diagram of Ge/SiGe quantum wells.

orbital in the xy plane as given in Eq. (6)

$$U(r) = \left(\frac{2}{\pi}\right)^{1/2} \frac{1}{\lambda} e^{-r/\lambda} \quad (6)$$

$$|U_{eh}(0)|^2 \propto \frac{2}{\pi} \left|\frac{1}{\lambda}\right|^2. \quad (7)$$

By minimizing the binding energy in such a variational approach, we can deduce the effective exciton radius, λ . Knowledge of λ allows us to deduce the scaling of the factor $|U_{eh}(0)|^2$ in Eq. (7). The location of the exciton peak is the valence subband to conduction subband separation energy, (E_{eh} in Eq. (8), as determined by transfer matrix method) less the binding energy (E_{Beh} in Eq. (8), as determined by the variational method). The strength of the 1S exciton absorption peak (i.e., the area under it in the absorption spectrum) is proportional to the product of $|U_{eh}(0)|^2$ (normalized to the strongest E1-HH1 transition at zero electric field, $|U_0(0)|^2$) and the step height (given by $|\langle \Psi_e | \Psi_h \rangle|^2$ [26]) with a 2.7×10^2 empirical scaling factor given by C in Eq. (8). (This scaling also presumes we can include the effects of any higher bound exciton states into this one approximate calculation.) As electric field is applied the step height will change, but so also will the (variationally determined) exciton effective radius, λ , leading to a further reduction in the exciton absorption peak area. For simplicity in our model, we treat the exciton peaks associated with the different valence to conduction subband pairs as if the exciton binding energy and radius was the same for each such pair. This is not strictly correct microscopically - in principle the exciton waveform and energy should be separately calculated for each valence and conduction subband pair - but we wish to keep the model relatively simple and such higher energy transitions are usually of less importance for device operation anyway. The final peak shape is defined by the inclusion of the empirically determined full width at half maximum (FWHM) that sets the width of the corresponding absorption line (given by the parameter Γ in Eq. (8)). For the line shape, we have empirically chosen to use a hyperbolic secant (sech) function because of its relatively good

agreement with experimental data. The FWHM includes homogeneous (e.g., from ultrafast carrier lifetimes [27]) and non-homogeneous broadening contributions (e.g., from well width fluctuations [19]). Characteristic exciton absorption peaks calculated this way are shown in Fig. 1 with the solid black line.

The same hyperbolic secant function is also used to convolve with the transition step since it is unphysical to have a sharp change in the electroabsorption profile because of short carrier lifetimes and layer thickness fluctuations. As a model approach therefore, we presume the same broadening effects apply both to the exciton absorption peak and to the other absorption processes, an approach that is at least reasonable as a first physical modeling approximation. This convolution is given by the dashed-dot black line in Fig. 1 (and the third line of Eq. (8)). The sum of the convolved steps and the effective 1S exciton peaks provides the QCSE spectra given by the dashed red line. The overall magnitude of the final simulated QCSE spectra has been scaled by an empirical factor of 3.3×10^{-9} for the E-HH ($h = HH$) transitions and a third that value for the E-LH ($h = LH$) transitions (B_h in Eq. (8)) to fit experimental data with units of cm^{-1} . Using this factor, we can fit electroabsorption data for a wide range of quantum wells and growth conditions as shown in Section IV.

The last model in SQWEAC is the indirect absorption (solid red line in Fig. 1 and $\alpha_{ind,t}$ in Eq. (8)), which is dominated by the Ge well material and is modeled following [20] with a 27.7 meV phonon energy. An in-depth discussion, including experimental data from photocurrent measurements, is given in [21]. Adding QCSE and indirect absorption gives the full simulated electroabsorption profile of the Ge/SiGe QWs at a given electric field. From experimental capacitance-voltage (CV) data, we found that the variation of electric field within the intrinsic region can be rather large (up to $\sim 1 \text{ V}/\mu\text{m}$) due to background doping of up to 10^{16} cm^{-3} . To compensate for this variation, we average three electroabsorption profiles corresponding to electric fields at the middle and edges of the i-region (given by the summation over t with $T = 3$ in Eq. (8)). The final SQWEAC calculation of the electroabsorption spectra at any electric field is given by Eq. (8)

$$\begin{aligned} \alpha_{total} = & \frac{1}{T} \sum_{t=1}^T \left\{ \sum_{e,h} \left[B_h |\langle \Psi_{e_t} | \Psi_{h_t} \rangle|^2 \times \left(C \frac{|U_{eh_t}(0)|^2}{U_0(0)^2} \right. \right. \right. \\ & \times A_s \text{sech} \left(\frac{E - E_{eh_t} - E_{B_{eh_t}}}{\Gamma_t} \right) \\ & \left. \left. \left. + \int_{E_{eh_t}}^{\infty} S_{2D}(E_0) A_s \text{sech} \left(\frac{E - E_0}{\Gamma_t} \right) dE_0 \right] \right. \\ & \left. \left. + \alpha_{ind,t}(E) \right\} \quad (8) \end{aligned}$$

where A_s is a normalization term for the hyperbolic secant function so $A_s \text{sech}(\cdot)$ has unit area, the summation over e and h is the sum over all electron and hole subbands of interest in our spectral range (including both light and heavy hole subbands) and E is the photon energy. Our model therefore has three empirically determined parameters, B_h , C , and Γ_t . Once chosen, the same values for B_h and C are

TABLE I

SAMPLE QW DESIGNS EXPERIMENTALLY TESTED AND COMPARED WITH SQWEAC. L1 GROWTHS WERE AT 500 °C WHILE Y GROWTHS WERE AT 400 °C. SAMPLES WERE STRAIN BALANCED TO THE VS WITH THE REPORTED VALUES DETERMINED BY SQWEAC AND EXPERIMENTAL STUDY

	Thickness (nm)		Composition (%Ge)			Number of QW periods
	Well	Barrier	Well	Barrier	VS	
L1G1	15.6	40 (± 4)	100	84	91	10
L1G5	14.0	~ 35	100	85	91	60
L1G6	19.5	~ 45	100	86	91	10
L1G7	23.3	~ 50	100	84	91	10
Y14	9.7	~ 16	100	86	90	15
Y19	9.8	~ 16	100	86	90	15
Y20	9.5	~ 16	100	86	90	15

used in all simulations for different samples. We change Γ_t as necessary for the samples due to differing well widths that may show different amounts of broadening from well thickness variations, and such thickness variations may also change from sample to sample.

III. GROWTH, FABRICATION AND EXPERIMENTAL SETUP

To validate our approach, which we call the Simple Quantum Well Electroabsorption Calculator, or SQWEAC for short, we took experimental data from the range of growths and material designs presented in Table I. (These numbers reflect the actual growth thicknesses of the samples. L1 growths for the wells, barriers and the virtual substrate were 150% to 200% thicker than designed depending on composition.) We will first discuss the technique used to measure absolute absorption spectra followed by a description of the material designs used to compare with the SQWEAC simulations.

A. Sample Growth and Fabrication

The samples we will compare were grown in two different epitaxial reduced-pressure chemical vapor deposition (RPCVD) machines at temperatures of 400 °C and 500 °C for the Y and L1 samples, respectively. A layer of B-doped $\text{Si}_{1-z}\text{Ge}_z$ of either $\sim 600 \text{ nm}$ or $\sim 1 \mu\text{m}$ thickness (Y and L1, respectively) was grown in two stages with higher temperature anneals at $\sim 800 \text{ °C}$ to reduce defect propagation into the active material and to create the virtual substrate (VS). For the L1 samples, a thin intrinsic spacer layer ($\sim 50 \text{ nm}$) of the same composition was grown prior to and following the quantum well (QW) region. The QW region consisted of a periodic structure of $\text{Ge}/\text{Si}_{1-x}\text{Ge}_x$ with a range of thicknesses. The final structure was capped by an As-doped $\text{Si}_{1-z}\text{Ge}_z$ layer to form the *pin* diode. The compositions and thicknesses for the L1 and Y samples are presented in Table I. The L1 growths had thicknesses that far exceeded ($\sim 2x$) the thickness specified by the original design, likely causing the structure not to be properly strain-balanced. However, even the samples with many quantum wells (such as L1G5) and thus very thick ($\sim 3 \mu\text{m}$) intrinsic regions still showed good QCSE behavior

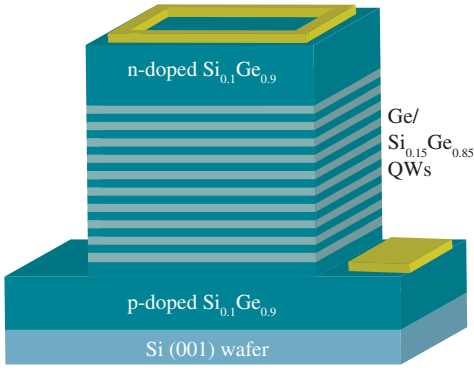


Fig. 3. Example QW structure in a *pin* diode used for photocurrent measurements.

[28]. We used measured overall thicknesses in calculating electric fields and absorption coefficients.

Following epitaxial growth, the photodiode mesas were lithographically defined and samples were etched to form a square mesa structure. Deposition of Ti/Al or Ti/Au ring contacts on the top and bottom of the mesa formed the n- and p-contacts (with $\sim 60 \Omega$ resistance, a sufficiently small value to neglect in electric field calculations) as shown in Fig. 3.

B. Experimental Setup

The experimental setup consisted of a tapered fiber tip lens to focus light, with an angular spread between 10° and 45° from normal to reduce Fabry-Perot fringes, onto the surface of the square mesa device. The data was calibrated to determine the amount of light that enters the device. The light sources were continuous wave lasers that gave a wavelength range of 1369 nm to 1641 nm (Agilent/HP 8164A). The full absorption spectra were taken using a lock-in (SRS830) with the laser being chopped at the source to give the necessary modulation for the lock-in and a low noise current pre-amplifier (SRS570) for supplying voltage and converting the photocurrent to voltage for measurement. These spectra were scaled to absolute absorption by measuring the d. c. photocurrent at specific wavelengths and voltages where there was a large contrast between light and dark d. c. current (i_{light} , i_{dark}) on a parameter analyzer (HP4145B). By separately measuring the absolute incident power (P_0) at these points, we can convert the resulting currents to the percent of light absorbed in the material using Eq. (9), where P_{abs} is the absorbed intensity of light and λ is the wavelength of the light. The (effective) absorption coefficient (or attenuation coefficient, α , in cm^{-1}) can be deduced using Eq. (10), where L is the thickness of the intrinsic region as determined by CV measurements. Hence, our effective absorption coefficients here are based on the entire thickness of the intrinsic region, which includes the well and barrier material (as well as spacers for the L1 growths)

$$\frac{P_{abs}}{P_0} = (i_{light} - i_{dark}) \cdot \frac{1.24}{\lambda} \cdot \frac{1}{P_0} \quad (9)$$

$$\frac{P_{abs}}{P_0} = 1 - e^{-\alpha L}. \quad (10)$$

IV. COMPARISON OF SQWEAC WITH EXPERIMENT

Using the simple calculator described in the theory section, we have compared the results against experimental data for L1 and Y samples (Table I). Figure 4 compares SQWEAC to the experimental results from Y14 and L1G1, which had different quantum well widths, compositions, growth temperatures and number of periods of QWs.

In order to model these very different test samples, we fit the transitions (E1-HH1, E1-HH2 and E2-HH1) by adjusting the well width, substrate composition and barrier composition. A very small range of values exist that can fit all these transitions and thus are essentially not free variables. Reference [12] gives typical ranges for these variables that still result in a good fit for all the transitions from experimental data. As an example of variation in growth, Y14, Y19 and Y20 were all originally designed to have a 10 nm well, but actual well widths ranged from 9.5 nm to 9.8 nm while the concentration of the substrate and barrier remained consistent. Following modeling of the transitions, the full electroabsorption profile is defined by adjusting the full width at half maximum (FWHM) to match that of experimental data. Typical values for the FWHM range from ~ 12 meV (Y samples) to ~ 16 meV (L1 samples) depending on the growth technique. We expect this variation for the different growths as many factors contribute to the linewidth (FWHM) of our hyperbolic secant profile. First, we know there must be a homogeneous component of ~ 3.6 meV from the known short lifetime of carriers in the central (direct) Ge conduction band valley [27]. Second, we expect there will be contributions from well width fluctuations, strain inhomogeneity from well to well (which may well occur in the L1 growths), and non-uniformity of the electric field across the i-region. The slight roughness due to the initial lattice mismatch between Si and the VS can propagate to cause < 1 nm variations in well thickness (as evident in the Y growths) and thus a broadening of the FWHM. The same well width fluctuations within a well affect small wells much more than large wells as a change of 0.1 nm is a much larger fraction of the well width for a small well, and confinement energies also tend to vary quadratically with the inverse of the well width.

SQWEAC gives very good agreement with the typical quantum well thickness of 10 nm (Fig. 4a). Even as we increase the well size to ~ 15.5 nm, we find good agreement between simulation and experiment (Fig. 4b). It is evident in SQWEAC as we move away from zone center (to higher energy transitions), the simulation does not fully predict the absorption in the experimental data. The first reason, especially for wider wells, is the tunneling resonance model does not simulate unbound states (for example, in Fig. 4b we do not simulate higher energy transitions at the largest electric field). Consequently, any transitions that are no longer bound (typically at larger electric fields) will not be included. The second reason for this difference is likely due to the known mixing of the s- and p-like unit cell states away from zone center. This mixing is calculated in the more sophisticated k-p [15] and tight-binding [13] models, which evaluate the entire momentum space and thus give better agreement at higher energies. For modulator

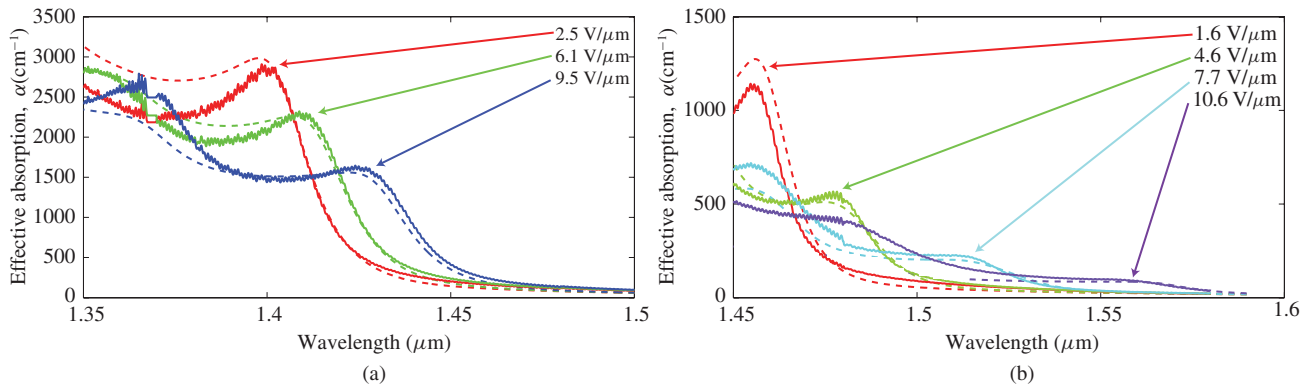


Fig. 4. Comparison of SQWEAC with experimental data for two different well sizes and growth conditions. Comparison of SQWEAC (dashed) with experimental data (solid) from (a) Y14 with ~ 10 nm well and (b) L1G1 with ~ 15.5 nm well. (The highest electric field curve at 10.6 V/ μm is truncated at wavelengths below ~ 1520 nm as SQWEAC only simulates the first E1-HH1 transition as higher transitions are unbounded for this well width and electric field.)

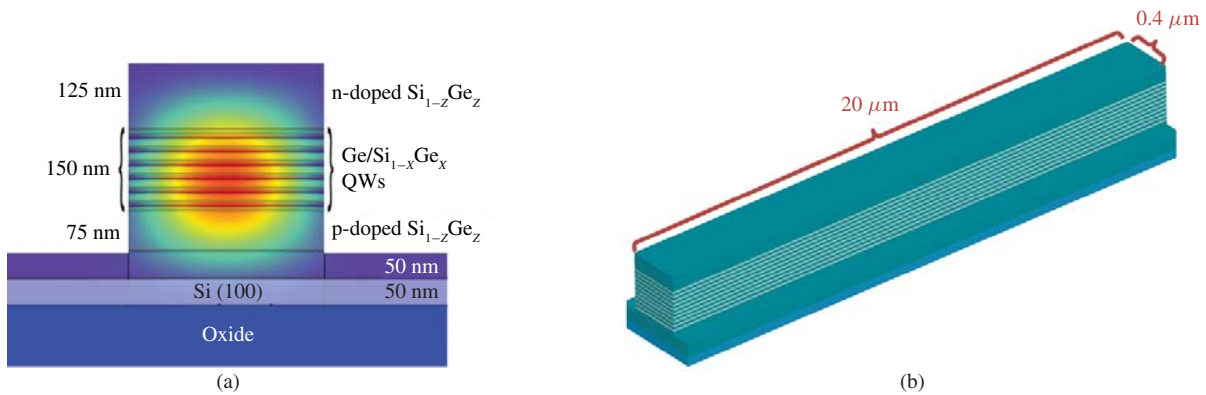


Fig. 5. (a) COMSOL simulation showing optical power overlap with the QWs of $\sim 57\%$. (b) Waveguide design giving < 8 fJ/bit.

design, the longer wavelength (lower energy) spectra to the first transition edge are the most important for deducing performance. SQWEAC has strong predictive power for these lower energy electroabsorption spectra and given the speed of simulation with the ability to include (or exclude) relevant physical properties, it is a very useful calculator to design electroabsorption modulators that can operate in the important communication wavelengths. In the next section, following a discussion of design considerations, we will present designs for 1310 nm and 1550 nm modulators expected to operate at ultralow power and high speed.

V. 1310 nm AND 1550 nm DESIGNS

Having demonstrated the viability of SQWEAC for predicting electroabsorption spectra for a range of quantum well widths and growth conditions, we can now implement SQWEAC to design electroabsorption modulators (EAMs) that can operate at the important communication wavelengths around 1310 nm and 1550 nm. In order to operate at these wavelengths, we must adjust the initial quantum well design from its nominal ~ 1450 nm operating wavelength. The material design choices include changing the composition of the substrate, barrier or even the well and adjusting the well width. We will begin this section by stepping through the effect of changing these four design components to shift operation

toward 1310 nm. We will then present the final 1310 nm and 1550 nm designs intended to operate with < 30 fJ/bit of energy.

In order to compare each of the four design choices, we will use the waveguide architecture presented in Fig. 5. Beginning with a silicon waveguide of 450 nm thickness and 400 nm width on oxide, a selective area $20 \mu\text{m}$ long is presumed to be etched to within 50 nm of the buried oxide to provide a Si(100) substrate for growth. Oxide is deposited on the vertical walls of the Si waveguide to prevent lateral growth (as previously demonstrated by Ren, *et al* [29]). The material would be selectively grown using reduced-pressure chemical vapor deposition (RPCVD) in a window that is wider than 400 nm. This dimension would provide a p-doped contact region (50 nm thick) as shown in the waveguide cross-section in Fig. 5a. In the same manner as presented in [30], the p-doped $\text{Si}_{1-z}\text{Ge}_z$ virtual substrate can be alternately grown and annealed to a total thickness of 125 nm selectively within the growth window. While the 125 nm virtual substrate (VS) is quite thin in comparison to previous published growths (such as [12], [31]), selective area growth of a thin 150 nm VS has still demonstrated QCSE [32]. Following the VS, a periodic structure of n well/barrier pairs of $\text{Si}_{1-y}\text{Ge}_y/\text{Si}_{1-x}\text{Ge}_x$ layers would then be grown to a thickness of 150 nm (where y is the composition of the well material and x is that of the barrier). The number of periods, n , is dependent on the composition

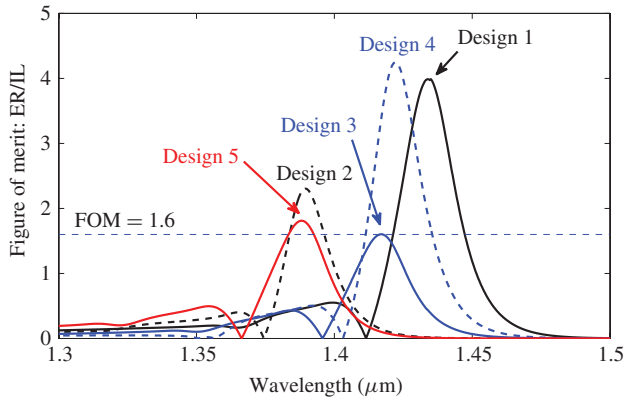


Fig. 6. FOM for the five design changes: Design 1 of nominal 10 nm pure Ge wells, 15% Si barrier, and 10% Si buffer, $n = 5$ (solid black), Design 2 with reduced 8 nm Ge well, $n = 6$ (dashed black), Design 3 with increased Si buffer of 13%, $n = 2$ (solid blue), Design 4 with increased Si barrier to 20%, $n = 8$ (dashed blue) and Design 5 with addition of Si in the well of 1%, $n = 5$ (solid red) compared with the FOM = 1.6. The zero points here refer to sign changes where the normally on-state becomes the off-state.

of the substrate, barrier and well material in addition to the well width choice for the 1310 nm and 1550 nm designs to maintain 150 nm total quantum well/barrier thickness and strain balancing. The final material would then be capped by a 125 nm n-doped $\text{Si}_{1-z}\text{Ge}_z$ to form the *pin* diode. Both n- and p-regions are designed with a doping concentration of 10^{18} cm^{-3} and the corresponding loss from (below band gap) absorption in doped materials is included according to the loss profile curves provided in [33], [34]. Following growth, the structure would be polished and etched to form the waveguide mesa. Oxide protection followed by contact vias and metal deposition would finalize the structure for testing. Simulations using COMSOL determined the overlap of the first-order optical mode (the only one present in these waveguides) with the QW region to be 58% and 57% of the total power for 1310 nm and 1550 nm wavelengths, respectively. The CV^2 energy consumption of such a 20 μm long waveguide using 0 V and 1 V biases ($\sim 4 \text{ V}/\mu\text{m}$ and $\sim 10.5 \text{ V}/\mu\text{m}$) is $< 8 \text{ fJ/bit}$ (or $\sim 0.4 \text{ fF}/\mu\text{m}$), which meets the energy requirements of even the shortest distance optical interconnects [1]. CV^2 would be the minimum total electrical energy to turn the modulator on and off again; under non-return-to-zero modulation, the average dissipated energy per bit would be half this number. Where possible, devices are designed for operating voltage swings of 1 V, a number that is compatible with direct drive by CMOS logic. In general with electroabsorption modulators, there is an additional dissipation energy E_{pc} from the electrical flow of the photogenerated charge through the device. This electrical dissipation will be $\sim V \times Q$ where V is the operating voltage and Q is the total photogenerated charge. The photogenerated charge in turn is bounded by the total optical energy being absorbed, E_{mod} , divided by the photon energy in electron volts ($\hbar\omega/q$) (we cannot generate more charge than would result from the total absorption of the input optical energy). So, the photocurrent dissipation energy is $\lesssim (V_e/\hbar\omega)E_{mod}$. If the operating voltage V is comparable to the photon energy in electron volts, then this photocurrent

TABLE II
QW DESIGNS DISCUSSED (DESIGNS 1–5) FOR SHIFTING TO 1310 nm OPERATING WAVELENGTH. ALSO PRESENTED ARE FINAL 1310 nm AND 1550 nm DESIGNS (VS). THE NUMBER OF QUANTUM WELLS IS DESIGNED TO FIT WITHIN THE 150 nm INTRINSIC THICKNESS (FOR $\sim 0.4 \text{ fF}/\mu\text{m}$) AS GIVEN IN THE DESIGN IN FIG. 5

Design	Thickness (nm)		Composition (%Ge)			Number of QW periods (n)
	Well	Barrier	Well	Barrier	VS	
1	10	20	100	85	90	5
2	8	16	100	85	90	6
3	10	65	100	85	87	2
4	10	10	100	80	90	8
5	10	18	99	85	90	5
1310 nm	7	4.2	99	75	90	13
1550 nm	14	7	100	85	95	7

electrical dissipation energy E_{pc} is comparable to the optical energy being absorbed. Specifically, for our two designs below, we would have, for 1 V drive and 0.8 eV (1.55 μm) photons $E_{pc} \lesssim 1.25 E_{mod}$, and for 2 V drive and 0.95 eV (1.3 μm) photons, $E_{pc} \lesssim 2.1 E_{mod}$. If we presume the system is run so that the modulator is on the average absorbing approximately half the input power, we can see in general that, under these conditions of relatively low operating voltage, the modulator photocurrent dissipation is comparable to or smaller than the input optical power being modulated. Hence, for such drive voltages, the photocurrent power dissipation is comparable to input optical power, roughly independent of the power being modulated. For larger bias voltages, beyond those in our designs below, photocurrent dissipation could become a dominant source of power dissipation, however. In the kind of balanced system design envisaged in Ref. [1], 10 fJ of optical energy would be modulated by a modulator with 1 V drive and 10 fF capacitance, so $\sim 10 \text{ fJ CV}^2$ energy, leading to $\sim 1 \text{ fJ}$ received optical energy after a total system loss of $\sim 10 \text{ dB}$. Such a 1 fJ/bit received energy is compatible with a receiverless (i.e., no input voltage amplification) design with a low ($\sim 1 \text{ fF}$) front end photodetector/transistor capacitance in an integrated technology. The photocurrent energy dissipation with 1 V drive would also then be $\lesssim 10 \text{ fJ}$. In the energy numbers below, we will quote only the CV^2 energies because the photocurrent dissipation energy depends on the design of the rest of the system, but the reader should understand there is such additional dissipation following our discussion here.

Parameters for various designs are given in Table II. In order to shift the operating wavelength from the nominal $\sim 1450 \text{ nm}$ (Design 1, similar to Y14) toward 1310 nm, we can decrease the well thickness (Design 2) or increase the Si content in the substrate (Design 3), barrier (Design 4) or even well material (Design 5). To compare these designs with the nominal design, a figure of merit (FOM) defined as the change in absorption divided by the absorption ($\Delta\alpha/\alpha$), which is equivalent to the extinction ratio over the insertion loss (ER/IL, where the IL is just the material loss), is used as it is independent of the length of the waveguide (given in Fig. 6). (Here by absorption we mean an effective absorption coefficient or equivalently the

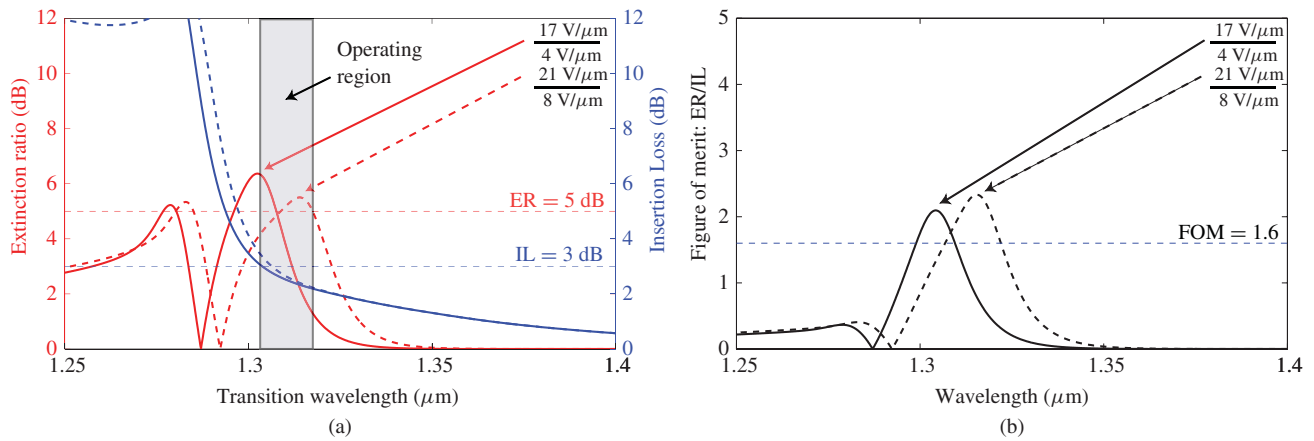


Fig. 7. 1310 nm modulator design with 7 nm well composed of $\text{Si}_{0.01}\text{Ge}_{0.99}/\text{Si}_{0.25}\text{Ge}_{0.75}$ well/barrier on $\text{Si}_{0.1}\text{Ge}_{0.9}$ VS ($n = 13$). (a) ER and IL and (b) FOM (ER/IL) for both 0 V and 0.6 V pre-bias with 2 V swing if it was in the waveguide architecture presented in Fig. 5, but with a 6 μm length instead of 20 μm . Corresponding energy consumption would be ~ 10 fJ/bit to ~ 15 fJ/bit for the 0 V and 0.6 V pre-biases, respectively.

transmission of the structure expressed in logarithmic units, such as decibels.) For shorter distance communication, we will use a target of >5 dB ER and <3 dB IL (or FOM >1.6). Such choices represent a reasonable balance between requiring significant contrast between the two states (a factor >3.3) while limiting the background loss to no more than 50%.

Design 2 shown by the dashed black line in Fig. 6 demonstrates the effects of reducing the well width to 8 nm (keeping all other parameters constant). This reduction increases the overlap of the electron and hole, even at high electric fields, but also reduces the shift in energy with field. With design 2, we are now able to fit 6 QWs in the 150 nm region (vs. 5 in the nominal design), increasing the ER. However, since the ER peak has a smaller shift towards longer wavelengths and the IL increases with the overall shift toward shorter wavelengths (by ~ 50 nm), we see an overall reduction in the FOM.

Adjusting the substrate composition to have more Si, as in Design 3 (solid blue line in Fig. 6) results in a much thicker barrier to maintain strain balancing. Consequently, only two periods of QWs can fit within 150 nm, causing the ER and FOM to reduce drastically without a strong shift to shorter wavelengths. However, increasing the Si in the barrier to 20% leads to a reduction in barrier width from 20 nm to 10 nm and thus an increase in the number of QWs to $n = 8$. For design 3, the ER increases significantly, though the shift to shorter wavelengths is minimal (as that shift only results from a slightly higher quantum confinement). It is clear that the effect of increasing the density of wells in the intrinsic region has a strong impact on the performance of the device with a slight increase in the FOM despite shifting to shorter wavelengths (dashed blue line in Fig. 6). Thus, an increase of Si composition in the barrier (within growth constraints) and a decrease in barrier thickness (maintaining a thickness in which coupling between wells does not dominate) is beneficial for future designs.

The final design is to put a small amount of Si in the well material (as opposed to leaving it as pure Ge). Since Si has a very large direct band gap of 4.0 eV, only a very small fraction is needed to shift toward higher energy (shorter wavelength).

Design 5 shows the effects of the addition of 1% Si in the well material (solid red line in Fig. 6). Similar to the 8 nm well from Design 2, the addition of 1% Si shifts the wavelength by ~ 50 nm though it gives a slightly smaller FOM. Unlike for the 8 nm well, the ER is slightly similar and number of QWs remains the same as the nominal design with a slight increase in the IL due to increasing indirect absorption at the shorter wavelengths (thus causing the reduction in the slight FOM).

To design a 1310 nm modulator, we can induce a strong shift in wavelength from ~ 1450 nm to ~ 1310 nm (a shift of ~ 140 nm) by reducing well width (to 7 nm) and adding Si (1%) to the well. The ER is improved by increasing in the number of QW periods ($n = 13$) due to higher Si barrier composition. Despite these design modifications, the insertion loss at 1310 nm from the indirect band edge is very strong. Thus, to achieve the FOM of >1.6 , we use a 2 V swing with either 0 V or 0.6 V pre-bias. With the stronger absorption (in both the on and off states), we can reduce the device length from 20 μm to 6 μm , giving energy dissipation of 10 fJ/bit and 15 fJ/bit for the 0 V and 0.6 V pre-biases, respectively (Fig. 7). The expected field across this device is quite high at 17 V/ μm and 21 V/ μm , though equivalent fields have been achieved with this Ge quantum well material system using selective area growth [30]. We can adjust the operating wavelength from 1300 nm to 1322 nm using the different pre-bias voltages while still maintaining the FOM criteria of 1.6 as shown in Figs. 7a and 7b. At the 6 μm length, the wavelength of operation would be between 1304 nm to 1317 nm while maintaining an ER > 5 dB and an IL < 3 dB. For this 1310 nm device, the energy consumption is much lower than the total energy of other Si-compatible modulators (if one includes the total power to tune resonator devices to any desired operating wavelength) at this wavelength of operation. It is not obvious that a viable FKE modulator can be constructed for 1310 nm in the SiGe material system. The indirect absorption is relatively much stronger at 1310 nm than at 1550 nm for both FKE and QCSE, but for FKE we do not expect larger absorption changes in the bulk SiGe material needed to push the direct absorption edge to this range.

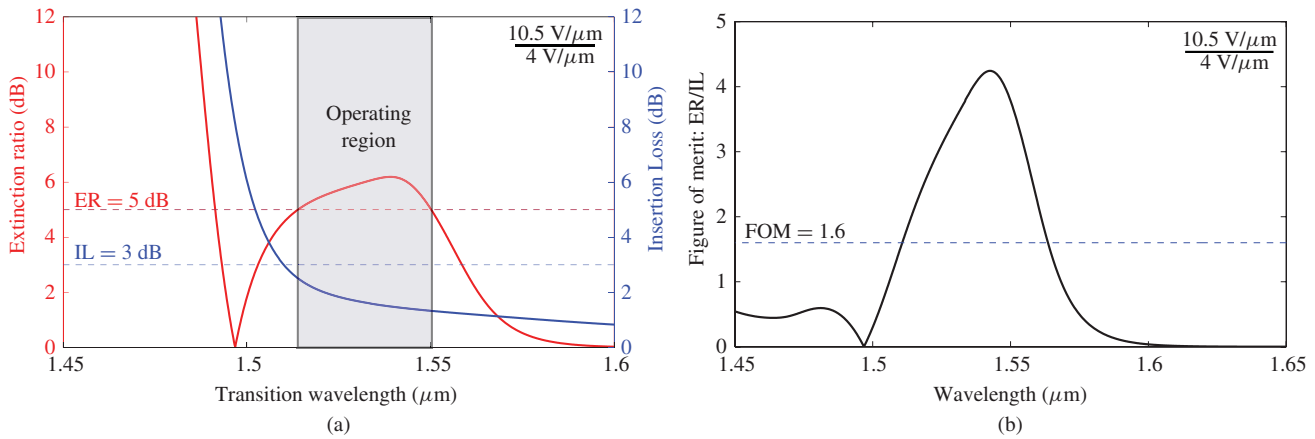


Fig. 8. 1550 nm modulator design with 14 nm well composed of $\text{Ge}/\text{Si}_{0.15}\text{Ge}_{0.85}$ well/barrier on $\text{Si}_{0.05}\text{Ge}_{0.95}$ VS ($n = 7$). (a) ER and IL. (b) FOM (ER/IL) for 0 V pre-bias with 1 V swing if it was in the waveguide architecture presented in Fig. 5, but with a 60 μm length instead of 20 μm . Corresponding energy consumption would be ~ 24 fJ/bit.

The flexibility of this QCSE material system also allows for the design of a (room temperature) 1550 nm modulator as shown in Fig. 8. In order to shift the operating wavelength toward longer wavelengths, we can reduce the compressive strain in the well material (and thus the direct band gap) by decreasing the Si composition in the VS from 10% to 5% (previously done experimentally by Kuo, *et al* [9]). To further shift toward lower energy (longer wavelength), we can increase the well width from 10 nm to 14 nm. We see the trend of a slight improvement in the FOM spanning a large wavelength range of ~ 50 nm from 1511 nm to 1563 nm (Fig. 8b). Slight improvement of the FOM is expected since the indirect absorption becomes less dominant at longer wavelengths (in contrast to its substantial increase as we shift toward 1310 nm). With the lower total absorption at 1550 nm, this device is slightly longer (60 μm) with a total energy consumption of ~ 24 fJ/bit. At this design length, the wavelength operation would be 1514 nm to 1550 nm for $ER > 5$ dB and $IL < 3$ dB. Further improvement in energy consumption could occur with increased Si in the barrier (which would reduce the barrier thickness), increasing the number of QWs in 150 nm. More QWs would increase the overall absorption and thus reduce the length of the device to maintain ER and IL.

VI. CONCLUSION

We have created a simple modeling approach, SQWEAC, which includes the various major physical effects present in the Ge QW material system and effectively fits the first transition (E1-HH1) for a range of material designs and growth conditions. For thinner wells, we experimentally see a strong enhancement in absorption due to excitonic effects while for larger wells we see that the excitonic effects are slightly weaker as predicted. While more sophisticated models exist for calculating the electronic band structure (e.g. k-p and tight-binding) or for including excitonic effects (e.g. the Green's function method), SQWEAC incorporates all of the relevant physical effects present in experimental structures, while improving the calculation speed. We found that indirect absorption, spectral broadening and the 1s exciton have a strong role in the electroabsorption spectra. The reliability and

speed of SQWEAC enables optimization of Ge-based quantum well structures for CMOS compatible low-power, high-speed, compact electroabsorption modulators. We have presented two such modulator designs that are predicted to operate at the important communication wavelengths of 1310 nm and 1550 nm with very small CV^2 energy consumption of 10 fJ/bit and 24 fJ/bit, respectively. The Ge/SiGe quantum well material structure in combination with SQWEAC provides a flexible platform for designing a wide array of modulator devices.

REFERENCES

- [1] D. A. B. Miller, "Device requirements for optical interconnects to silicon chips," *Proc. IEEE*, vol. 97, no. 7, pp. 1166–1185, Jul. 2009.
- [2] L. Liao, A. Liu, D. Rubin, J. Basak, Y. Chetrit, H. Nguyen, R. Cohen, N. Izhaky, and M. Paniccia, "40 Gbit/s silicon optical modulator for highspeed applications," *Electron. Lett.*, vol. 43, no. 22, pp. 1156–1157, Oct. 2007.
- [3] W. M. Green, M. J. Rooks, L. Sekaric, and Y. A. Vlasov, "Ultracompact, low RF power, 10 Gb/s silicon Mach-Zehnder modulator," *Opt. Exp.*, vol. 15, no. 25, pp. 17106–17113, 2007.
- [4] W. A. Zortman, M. R. Watts, D. C. Trotter, R. W. Yong, and A. L. Lentine, "Low-power high-speed silicon microdisk modulators," in *Proc. Conf. Lasers Electro-Opt.*, San Jose, CA, May 2010, no. CThJ4, pp. 1–2.
- [5] M. R. Watts, W. A. Zortman, D. C. Trotter, G. N. Nielson, D. L. Luck, and R. W. Yong, "Adiabatic resonant microrings (ARMs) with directly integrated thermal microphotronics," in *Proc. Conf. Lasers Electro-Opt.*, Baltimore, MD, Jun. 2009, no. CPDB10, pp. 1–2.
- [6] J. Liu, M. Beals, A. Pomerene, S. Bernardis, R. Sun, J. Cheng, L. C. Kimerling, and J. Michel, "Waveguide-integrated, ultralow-energy GeSi electro-absorption modulators," *Nature Photon.*, vol. 2, pp. 433–437, May 2008.
- [7] N.-N. Feng, D. Feng, S. Liao, X. Wang, P. Dong, H. Liang, C.-C. Kung, W. Qian, J. Fong, R. Shafiqi, Y. Luo, J. Cunningham, A. V. Krishnamoorthy, and M. Asghari, "30GHz Ge electro-absorption modulator integrated with 3 μm silicon-on-insulator waveguide," *Opt. Exp.*, vol. 19, no. 8, pp. 7062–7067, Apr. 2011.
- [8] Y.-H. Kuo, Y. K. Lee, S. R. Y. Ge, J. E. Roth, T. I. Kamins, D. A. B. Miller, and J. S. Harris, "Strong quantum-confined Stark effect in germanium quantum-well structures on silicon," *Nature*, vol. 437, pp. 1334–1336, Oct. 2005.
- [9] Y.-H. Kuo, Y. K. Lee, Y. Ge, S. Ren, J. E. Roth, T. I. Kamins, D. A. B. Miller, and J. S. Harris, "Quantum-confined Stark effect in Ge/SiGe quantum wells on Si for optical modulators," *IEEE J. Sel. Topics Quantum Electron.*, vol. 12, no. 6, pp. 1503–1513, Nov.–Dec. 2006.
- [10] Y. Rong, Y. Ge, Y. Huo, M. Fiorentino, M. R. T. Tan, T. I. Kamins, T. J. Ochalski, G. Huyet, and J. S. Harris, "Quantum-confined Stark effect in Ge/SiGe quantum wells on Si," *IEEE J. Sel. Topics Quantum Electron.*, vol. 16, no. 1, pp. 85–92, Jan.–Feb. 2010.

- [11] S. Ren, Y. Rong, S. A. Claussen, R. K. Schaevitz, T. I. Kamins, J. S. Harris, and D. A. B. Miller, "A Ge/SiGe quantum well waveguide modulator monolithically integrated with SOI waveguides," in *Proc. IEEE Group IV Photon.*, London, U.K., Sept. 2011, no. WA3.
- [12] R. K. Schaevitz, J. E. Roth, S. Ren, O. Fidaner, and D. A. B. Miller, "Material properties of Si-Ge/Ge quantum wells," *IEEE J. Sel. Topics Quantum Electron.*, vol. 14, no. 4, pp. 1082–1089, Jul.–Aug. 2008.
- [13] M. Virgilio and G. Grosso, "Quantum-confined Stark effect in Ge/SiGe quantum wells: A tight-binding description," *Phys. Rev. B*, vol. 77, no. 16, p. 165315, Apr. 2008.
- [14] M. Virgilio, M. Bonfanti, D. Chrastina, A. Neels, G. Isella, E. Grilli, M. Guzzi, G. Grosso, H. Sigg, and H. Kanel, "Polarization-dependent absorption in Ge/SiGe multiple quantum wells: Theory and experiment," *Phys. Rev. B*, vol. 79, no. 7, pp. 075323-1–075323-6, Feb. 2009.
- [15] D. J. Paul, "8-band k-p modeling of the quantum confined Stark effect in Ge quantum wells on Si substrates," *Phys. Rev. B*, vol. 77, no. 15, pp. 155323-1–155323-7, 2008.
- [16] L. Lever, Z. Ikonik, A. Valavanis, J. D. Cooper, and R. W. Kelsall, "Design of Ge–SiGe quantum-confined Stark effect electroabsorption heterostructures for CMOS compatible photonics," *J. Lightw. Technol.*, vol. 28, no. 22, pp. 3273–3281, Nov. 2010.
- [17] L. Lever, Z. Ikonik, A. Valavanis, and R. W. Kelsall, "Design of Ge/SiGe quantum-confined Stark effect modulators for CMOS compatible photonics," *Proc. SPIE*, vol. 7606, pp. 76060Q-1–76060Q-9, Jan. 2010.
- [18] S.-L. Chuang, S. Schmitt-Rink, D. A. B. Miller, and D. S. Chemla, "Exciton Green's-function approach to optical absorption in a quantum well with an applied electric field," *Phys. Rev. B*, vol. 43, no. 2, pp. 1500–1509, Jan. 1991.
- [19] D. S. Chemla, D. A. B. Miller, P. W. Smith, A. C. Gossard, and W. Wiegmann, "Room temperature excitonic nonlinear absorption and refraction in GaAs/AlGaAs multiple quantum well structures," *IEEE J. Quantum Electron.*, vol. 20, no. 3, pp. 265–275, Mar. 1984.
- [20] A. Frova, P. Handler, F. A. Germano, and D. E. Aspnes, "Electroabsorption effects at the band edges of silicon and germanium," *Phys. Rev.*, vol. 145, no. 2, pp. 575–583, 1966.
- [21] R. K. Schaevitz, D. S. Ly-Gagnon, J. E. Roth, E. H. Edwards, and D. A. B. Miller, "Indirect absorption in germanium quantum wells," *AIP Adv.*, vol. 1, no. 3, pp. 032164-1–032164-12, 2011.
- [22] S. Kodama, T. Yoshimatsu, and H. Ito, "500 Gbit/s optical gate monolithically integrating photodiode and electroabsorption modulator," *Electron. Lett.*, vol. 40, no. 9, pp. 555–556, Apr. 2004.
- [23] D. A. B. Miller, J. S. Weiner, and D. S. Chemla, "Electric-field dependence of linear optical properties in quantum well structures: Waveguide electroabsorption and sum rules," *IEEE J. Quantum Electron.*, vol. 22, no. 9, pp. 1816–1830, Sep. 1986.
- [24] D. A. B. Miller, *Quantum Mechanics for Scientists and Engineers*. Cambridge, U.K.: Cambridge Univ. Press, 2008.
- [25] Y.-H. Kuo and Y.-S. Li, "Variational calculation for the direct-gap exciton in the Ge quantum well systems," *Phys. Rev. B*, vol. 79, no. 24, pp. 245328-1–245328-8, 2009.
- [26] D. A. B. Miller, D. S. Chemla, T. C. Damen, A. C. Gossard, W. Wiegmann, T. H. Wood, and C. A. Burrus, "Electric field dependence of optical absorption near the band gap of quantum-well structures," *Phys. Rev. B*, vol. 32, no. 2, pp. 1043–1060, Jul. 1985.
- [27] S. A. Claussen, E. Tasyurek, J. E. Roth, and D. A. B. Miller, "Measurement and modeling of ultrafast carrier dynamics and transport in germanium/silicon-germanium quantum wells," *Opt. Exp.*, vol. 18, no. 25, pp. 25596–25607, Dec. 2010.
- [28] J. E. Roth, O. Fidaner, R. K. Schaevitz, Y.-H. Kuo, T. I. Kamins, J. S. Harris, and D. A. B. Miller, "Optical modulator on silicon employing germanium quantum wells," *Opt. Exp.*, vol. 15, no. 9, pp. 5851–5859, 2007.
- [29] S. Ren, T. I. Kamins, and D. A. B. Miller, "Thin dielectric spacer for the monolithic integration of bulk germanium or germanium quantum wells with silicon-on-insulator waveguides," *IEEE Photon. J.*, vol. 3, no. 4, pp. 739–747, Aug. 2011.
- [30] S. Ren, Y. Rong, T. I. Kamins, J. S. Harris, and D. A. B. Miller, "Selective epitaxial growth of Ge/Si_{0.15}Ge_{0.85} quantum wells on Si substrate using reduced pressure chemical vapor deposition," *Appl. Phys. Lett.*, vol. 98, no. 15, pp. 151108-1–151108-3, Apr. 2011.
- [31] E. H. Edwards, R. M. Audet, Y. Rong, S. A. Claussen, R. K. Schaevitz, E. Tasyurek, S. Ren, T. I. Kamins, O. I. Dosunmu, M. S. Ünlü, J. S. Harris, and D. A. B. Miller, "Si-Ge surface-normal asymmetric Fabry-Perot quantum-confined stark effect electroabsorption modulator," in *Proc. IEEE Photon. Soc. Summer Topical Meet.*, Playa del Carmen, Mexico, Jul. 2010, no. TuD2.4, pp. 211–212.
- [32] S. Ren, "Ge/SiGe quantum well waveguide modulator for optical interconnect systems," Ph.D. dissertation, Dept. Elect. Eng., Stanford Univ., Stanford, CA, 2011.
- [33] R. Newman and W. W. Tyler, "Effect of impurities on free-hole infrared absorption in p-type germanium," *Phys. Rev.*, vol. 105, no. 3, pp. 885–886, 1957.
- [34] W. G. Spitzer, F. A. Trubore, and R. A. Logan, "Properties of heavily doped n-type germanium," *J. Appl. Phys.*, vol. 32, no. 10, pp. 1822–1830, Oct. 1961.



Rebecca K. Schaevitz received the B.S. degree from Tufts University, Medford, MA, in 2008, and the M.S. and Ph.D. degrees from Stanford University, Stanford, CA, in 2008 and 2011, respectively. Her thesis is titled Electroabsorption Mechanisms in Germanium Quantum Well Material.

She has received the National Science Foundation's Graduate Research Fellowship in addition to the Intel Fellowship while at Stanford. As a Student Member of the Optical Society of America and the International Society for Optical Engineering, she

has helped to organize invited lectures and planned the inaugural Stanford University Photonics Retreat as Vice President of the Chapter.



Elizabeth H. Edwards (M'02) received the B.S. degree in electrical engineering from the University of Illinois, Chicago, and the M.S. degree in electrical engineering from Stanford University, Stanford, CA, in 2003 and 2008, respectively. She is currently pursuing the Ph.D. degree in electrical engineering with Stanford University.

She joined the Engineering and Technology Services Department, IBM, San Jose, CA, in 2003, where she was involved in application-specific integrated circuit design for various projects including

the Blue Gene P supercomputer. Her current research interests include photonic interconnects.



Jonathan E. Roth received the B.S. degree in biomedical engineering from Case Western Reserve University, Cleveland, OH, in 2000, and the Ph.D. degree in electrical engineering from Stanford University, Stanford, CA, in 2007, with a thesis titled Electroabsorption Modulators for CMOS Compatible Optical Interconnects in III–V and Group IV Materials.

He was with the Lund Institute of Technology, Lund, Sweden, from 2000 to 2001, on a Fulbright Fellowship. He is currently with Aurion, Inc.,

Goleta, CA, designing devices for photonic integrated circuits on a hybrid platform combining III–V active components and silicon waveguides.



Edward T. Fei received the B.S. degree in physics from Stanford University, Stanford, CA, in 2007. He is currently pursuing the M.S. and Ph.D. degrees in electrical engineering with the same university.

His current research interests include photonic interconnects and hetero-epitaxy of Ge on Si.

Mr. Fei has received the National Science Foundation's Graduate Research Fellowship in addition to the Stanford Graduate Fellowship. He was awarded the Electronic Materials Symposiums Undergraduate Award in 2007 and the Pan Wen Yuan Foundation

Scholarship in 2008.



Yiwen Rong received the B.S. degree in electrical engineering from the Harbin Institute of Technology, Harbin, China, in 2005, and the M.S. and Ph.D. degrees in electrical engineering from Stanford University, Stanford, CA, in 2007 and 2010, respectively.

He is currently a Senior Product Development Engineer with Philips Lumileds, San Jose, CA. His current research interests include GaN on sapphire, GaN on Si semiconductor devices, and front end and back end process engineering for III-V material

semiconductors.



Pierre Wahl received the B.S. degree in electrical engineering and the M.S. degree in erasmus mundus in photonics from Vrije Universiteit Brussel, Brussels, Belgium, in 2007 and 2010, respectively. During his Masters degree, he visited Kungliga Tekniska Hgskolan, Stockholm, Sweden, as a Visiting Student in 2009. He completed his Masters thesis with Interuniversity Microelectronics Centre, Leuven, Belgium, in 2010, on high frequency electrical voltage-controlled oscillators. He is currently pursuing the Ph.D. degree in electrical engineering

with Vrije Universiteit Brussel.

He joined the Miller Group, Stanford University, Stanford, CA, as a Visiting Researcher from 2010 to July 2011. His current research interests include optical interconnects, advanced simulation, and optimization methods in nanophotonics.

Mr. Wahl is a member of the International Society for Optical Engineering since 2010. In 2009, he served as the President of the local group of the Board of European Students of Technology in Stockholm.



Theodore I. Kamins (F'91) received the degree from the University of California, Berkeley.

He is a Consulting Professor with the Electrical Engineering Department, Stanford University, Stanford, CA, where he is a Guiding Researcher on epitaxial Si and Ge deposition for optical interconnects, on photodiode arrays for retinal prosthesis, and other advanced semiconductor processing. He joined the Research and Development Laboratory of Fairchild Semiconductor, University of California, where he worked with epitaxial and polycrystalline silicon

before moving to Hewlett-Packard Laboratories, Palo Alto, CA, working on numerous semiconductor material and device topics. Most recently at Hewlett-Packard Laboratories, he was a Principal Scientist with Information and Quantum Systems Laboratory, where he conducted research on advanced nanostructured electronic and sensing materials and devices. He is co-author with R. S. Muller of the textbook *Device Electronics for Integrated Circuits* and is author of the book *Polycrystalline Silicon for Integrated Circuits and Displays*.

Mr. Kamins is a fellow of the Electrochemical Society. He has taught with the University of California and Stanford University and has been an Associate Editor of the IEEE TRANSACTIONS ON ELECTRON DEVICES.



James S. Harris (S'65–M'69–SM'78–F'88–LF'07) received the B.S., M.S., and Ph.D. degrees in electrical engineering from Stanford University, Stanford, CA, in 1964, 1965, and 1969, respectively.

He is the James and Ellenor Chesebrough Professor of electrical engineering, applied physics, and materials science with Stanford University. In 1969, he joined Rockwell International Science Center, Thousand Oaks, CA, where he was one of the key contributors to ion implantation, molecular beam epitaxy, and heterojunction devices, leading to their preeminent position in GaAs technology. In 1980, he became the Director of the Optoelectronics Research Department. In 1982, he joined the Solid State Electronics Laboratory, Stanford University, as a Professor of electrical engineering. He has supervised more than 105 Ph.D. students. He is the author or co-author of more than 850 publications and holds 28 issued U.S. patents. His current research interests include physics and application of ultra-small structures and novel materials to new high-speed and spin-based electronics, optoelectronic devices, and systems.

Dr. Harris served as the Director of the Solid State Electronics Laboratory from 1984 to 1998 and the Joint Services Electronics Program from 1985 to 1999. He is a member of the National Academy of Engineering, a fellow of the American Physical Society, the Optical Society of America, and the Materials Research Society. He received the IEEE Morris N. Liebmann Memorial Award in 2000, the International Compound Semiconductor Conference Walker Medal in 2000, an IEEE Third Millennium Medal, the Alexander von Humboldt Senior Research Prize in 1998, and the International MBE Conference MBE Innovator Award in 2008 for his contributions to compound semiconductor materials, devices, and technology.



David A. B. Miller (F'95) received two Honorary degrees and the Ph.D. degree in physics from Heriot-Watt University, Edinburgh, U.K., in 1979.

He was with Bell Laboratories, Murray Hill, NJ, from 1981 to 1996, as a Department Head from 1987. He is currently the W. M. Keck Professor of electrical engineering and a Co-Director of the Stanford Photonics Research Center, Stanford University, Stanford, CA. He has published more than 230 scientific papers and the textbook *Quantum Mechanics for Scientists and Engineers* and holds 69

patents. His current research interests include physics and devices in nanophotonics, nanometallics, quantum-well optoelectronics, and fundamentals and applications of optics in information sensing, switching, and processing.

Dr. Miller has received numerous awards. He is a fellow of the Optical Society of America, the American Physical Society, and the Royal Societies of Edinburgh and London, a member of the National Academy of Sciences and the National Academy of Engineering.